

Analysis of morphological and haemodynamical indexes in abdominal aortic aneurysms as preliminary indicators of intraluminal thrombus deposition

Claudia M. Colciago · Simone Deparis* · Maurizio Domanin · Chiara Riccobene · Elisa Schenone · Alfio Quarteroni

Accepted: Nov 20th 2019

Abstract In this paper we study the correlation between the Wall Shear Stress (WSS), a haemodynamical index derived from numerical simulations, and an new index MFA-ILT for the characterisation of intraluminal thrombus (ILT) in presence of abdominal aortic aneurysms. Based on the processing of medical images, we define our index MFA-ILT by projecting onto lumen surface a measure of the ILT thickness. From the physical point of view, haemodynamical indexes describe the mechanical stimuli at which the luminal surface of the vessel wall is subject to, due to blood flow. Specifically, we consider the time-averaged wall shear stress and the oscillatory shear index. The first index provides a measurement of the averaged magnitude of the shear stress; the second index measures the rate of change of shear stress. To reconstruct the haemodynamical indexes, we build *in silico* three-dimensional models. We use the same physical parameters and boundary conditions for all the aneurysms in the sample. The computer simulations do not require any additional invasive patient examination.

We consider eleven cases of abdominal aortic aneurysms spanning a wide range of different morphological features. All the cases are characterized by a thin intraluminal thrombus. We can, therefore, assume that the lumen we currently observe does not significantly differ from the one before the thrombus deposition. Our results suggest that the value of wall shear stresses and intraluminal thrombus deposition are correlated. Moreover, we conclude that in six cases time-averaged wall shear stress provides a preliminary indication of the area at risk of thrombus deposition.

Keywords Haemodynamics · abdominal aortic aneurysm · intraluminal thrombus · wall shear stress · oscillatory shear index

C. Colciago

Chair of Modelling and Scientific Computing, EPFL Lausanne, Station 8, CH-1015 Lausanne, Switzerland E-mail: cmcolciago@gmail.com

S. Deparis*

SCI-SB-SD, Institute of Mathematics, EPFL Lausanne, Station 8, CH-1015 Lausanne, Switzerland E-mail: simone.deparis@epfl.ch

M. Domanin

Department of Clinical Sciences and Community Health, Università di Milano, Via della Commenda 19 Milan, Italy, and Unità Operativa di Chirurgia Vascolare, Fondazione I.R.C.C.S. Cà Granda Ospedale Maggiore Policlinico, Via Francesco Sforza 35 Milan, Italy E-mail: maurizio.domanin@unimi.it

C. Riccobene

Moxoff spa, Via durando 38A, Milano, Italy E-mail: chiara.riccobene@moxoff.com

E. Schenone

Moxoff spa, Via durando 38A, Milano, Italy E-mail: elisa.schenone@moxoff.com

A. Quarteroni

MOX, Department of Mathematics, Politecnico di Milano, Piazza Leonardo da Vinci, 32, 20133 Milan, Italy and EPFL, Lausanne, Switzerland (honorary professor) E-mail: alfio.quarteroni@polimi.it

1 Introduction

Abdominal Aortic Aneurysm (AAA) is a vascular pathology that affects up to the 8% of the population over 65 years old. An abdominal aneurysm is defined as an aortic diameter at least one to 1.5 times the normal diameter at the level of the renal arteries, which is approximately 2.0 cm. Thus, generally, a segment of abdominal aorta with a diameter larger than 3.0 cm is considered an AAA [11]. The presence of an AAA may lead to the rupture of the arterial wall, which causes death in the 80%-90% of the cases [40,5]. When analyzing patients conditions, clinicians are mainly interested in assessing the risk of rupture. This risk is related to several factors: wall stress, wall strength, aneurysm expansion rate, and deposition of IntraLuminal Thrombus (ILT) [28].

Nowadays, the main quantitative criterion to assess the rupture risk is represented by the maximum diameter: if the aneurysm diameter is greater than 5.5 cm, guidelines recommend elective repair for patient with a low or acceptable surgical risk [12,1]. Despite this criterion has proven not to be the best predictive choice [18,29,24,15], it is still widely used as the aneurysm diameter can be directly recovered from medical images and is still considered as the golden standard in the current practice. Other bio-mechanical and hemodynamical indices have been proposed in literature. For example, bio-mechanical rupture risk predictors have been developed based on the wall stress assessment and the comparisons between stress and strength[45,48,37]. More recently, also the analysis of the pulsatile blood flow that act during the cardiac cycle, have been considered as potentially involved in AAA formation and development [4], using magnetic resonance twice in a 2- to 3-yr interval reported that regions of low OSI had the strongest correlation with ILT growth and demonstrated a statistically significant correlation coefficient. Lozowy et al [34] reported the creation of turbulent vortex structures along the anterior wall and recirculating blood along the posterior wall.

An important role in aneurysms' assessment is played by the ILT. Its role is indeed still under discussion: on one side, it is thought to lower the rupture risk as its presence results in a lowering of the mechanical stress [52]; on the other side, also the strength of the arterial wall is diminished by the deposition of ILT [49]. Regarding the prediction of ILT deposition, rather than on mechanical stresses inside the vessel wall, the focus shifts on haemodynamical shear stresses on the lumen wall [17,16,47,19,9,31].

Despite their undoubted significance from a physical point of view, these indexes are still not employed in current clinicians' activities: in fact the stresses, whether bio mechanical or hemodynamical, are rather difficult to be measured *in vivo* without performing invasive patients examinations. Nevertheless, these indexes can be computed, non invasively, through numerical solutions of mathematical flow models. Despite this advantage, mathematical models present a high level of complexity and they involve severe computational costs (they may involve hours on cluster computers [14]). Justification of their usage demands therefore to demonstrate the efficacy of computer simulations from a clinical point of view. The quality of the numerical results strongly depends on the quality of input patient-specific data. For the setup of accurate simulations, it is of primary importance the reconstruction of three dimensional patient-specific geometries. This morphological information can be extracted from Digital Imaging and Communications in Medicine (DICOM) series of images. DICOM images result from Computed Tomography Scanning (CT-scan), a common practice performed on patients affected by AAA. The geometry is not the only information required for the setup of patient-specific models. Flowrates and/or pressures data at specific location are also needed. Differently from the geometry, these data are not typically collected during the standard examinations (in particular pressure, which uses invasive procedures).

In the authors' opinion, finding and computing simulation-based risk indicators that do not require extensive patient-specific data could support the clinicians in their preliminary assessment of the patient's condition. Purely haemodynamical studies have been conducted to compare simulation results and real data on very small samples of aneurysms [46,41,33,26,25] (maximum 5 cases). These works focus on the fluid flow, neglecting the presence of a compliant structure surrounding the blood and, thus, assuming as rigid the vessel wall. It has to be noted that the quantities of interest in these studies should be measured specifically on the moving interface between blood and vessel wall. Supposing a rigid wall may arise in significantly different wall shear

stress computations, as already shown in other vascular applications [13, 7]. Fluid-Structure Interaction (FSI) models are more adherent to the real situation featuring the description of a coupled system composed by the blood flow and the vessel wall in a moving domain (see e.g. [27]). Being more complex, FSI problems are also more demanding from the computational costs point of view. In this work, we compromise between rigid and FSI model choosing a fluid model enriched by a membrane-like condition on the lumen surface [13]. The mathematical complexity of our model is as the rigid wall one while we gain accuracy where we are interested in reconstructing the indexes.

We aim at emphasizing the importance of haemodynamical numerical simulations in assessing the risk of ILT deposition. We select a sample of AAA presenting a thin ILT such that we can assume that the current geometry of the *lumen* is close enough to the one before ILT deposition. We also suppose that the areas where we observe a thin ILT correspond to areas where the ILT deposition will continue to grow. Based on these two assumptions, we show that the risk of ILT deposition is correlated to the magnitude of the wall shear stress. We investigate this relation using patient-specific geometries, derived from CT-scan images, and averaged-population flowrate data. This choice for the simulation settings allows us to easily repeat the computations on any patient for which CT-scans data are available.

In Section 2 we introduce the algorithm used to segment the aneurysms and we discuss the characteristics of the selected sample. In Section 3 we describe the mathematical model that we use for the simulation of the blood flow and the setup of the algebraic equations' solver is discussed. In Section 4 we introduce main indices that we consider to measure ILT deposition. Results and comparisons are presented in Section 5. Conclusions follow.

2 Geometrical model

Abdominal aortic aneurysms present an extremely wide morphological variability from patient to patient. Some of the geometrical characteristics are key factors when considering the criticality of the patient's conditions [44]. Nevertheless, nowadays, the importance of these additional morphological features is assessed mainly on the ground of the clinician's experience. A first geometrical differentiation factor among AAAs can be defined by the shape of the aneurysm's sac: in the majority of the cases it is possible to distinguish between *fusiform* aneurysms and *saccular* shaped aneurysms. Another relevant morphological feature is represented by the *neck* of the aneurysm, defined as the portion of the aorta that starts right below the renal bifurcation and ends where the aneurysm's sac begins. The morphological characteristics of the neck can be a key factor to determine how the blood flow impinges on the aneurysm's sac and, thus, on the dynamics of the pattern of the wall shear stress along the heartbeat. The classification of AAAs shape was defined according to [2, (Table 1)]. Software aXurge was used for qualitative assessment of imaging data sets; this task was done by a clinician expert in reading CTA imaging (MD) according to [30, Table 1].

On a data set of about a hundred of AAAs, we select eleven aneurysms with a common feature: they present a thin ILT on, at least, a portion of the aneurysm, cf Table 1. The small number of selected cases is due to the fact that AAAs are usually detected in an advanced stage (they are usually asymptomatic) when there is already a significant deposition of ILT.

Using an automatic segmentation algorithm [20] based on three-dimensional vessel segmentation and connected component localization [22], we reconstruct all the eleven lumen surfaces (see Figure 3). The input data of the segmentation procedure are represented by DICOM series of images. The algorithm requires only a minimal level of user interaction. In fact, the user is asked to select five points, delimiting the target domain (see Figure 1):

1. **aorta** marker point, to be selected inside the aorta's lumen right below the renal bifurcation;
2. **left iliac** marker point, to be selected inside the lumen of the left iliac located at the left iliac bifurcation;
3. **right iliac** marker point, to be selected inside the lumen of the right iliac located at the right iliac bifurcation;

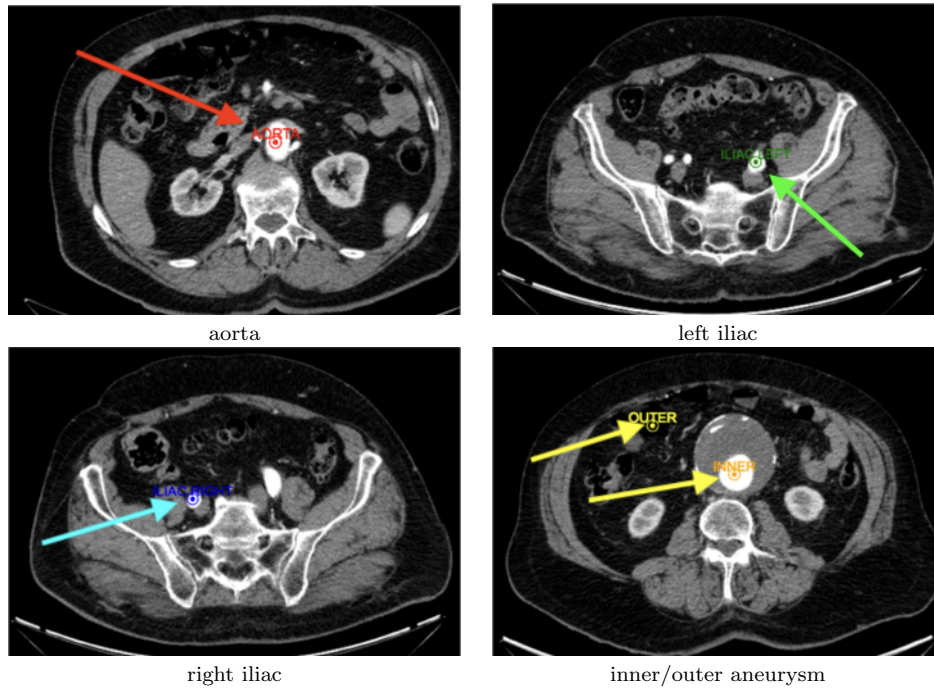


Fig. 1: Markers selection on the DICOM images as performed with aXurge software.

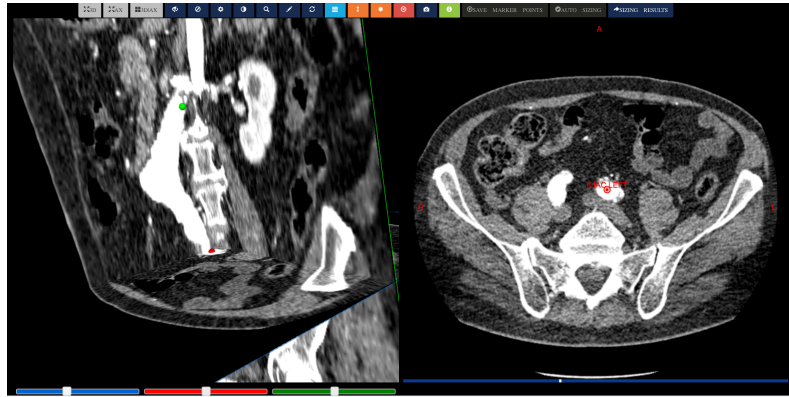


Fig. 2: 3D visualization of DICOM images and marker points with aXurge software.

4. **inner aneurysm** marker point, to be selected inside the aneurysm lumen, approximately at the center of the largest diameter location;
5. **outer aneurysm** marker point, to be selected outside the aneurysm lumen, approximately where the gray scale is significantly different from the one of the lumen.

A user with a medical expertise can easily detect these points exploring the DICOM images. Moreover, aXurge software also allows to check the position of the marker points with a 3D visualization of the DICOM images (see Figure 2). The automatic segmentation algorithm described

in [22] is based on three main steps an has been modified only in the choice of the initialization points and thresholds as follows:

1. Identification of Volume of Interest (VOI) based on the position of the four points related to the lumen of the vessel;
2. Creation of a feature image based on a combination of threshold and colliding fronts algorithms. The five points are used to set the threshold values computing the mean intensity around them. The aorta and the left and right iliac points are respectively the source and the targets for the colliding fronts algorithm;
3. Level set segmentation, initialized by the previously computed feature image. A median filter of kernel 1 is also applied to reduce the noise of the original image.

The purpose is the identification of the vascular district we aim at reconstructing and performing haemodynamical simulations. The results are presented in Figure 3. We notice that all the domains are characterized by one *inlet* surface, at the level of the infrarenal aorta, and two *outlet* surfaces, corresponding to those locations where each iliac artery branches in internal and external iliac. Several of the key morphological characteristics that can be encountered when dealing with abdominal aneurysms are well represented in our sample. In fact, we observe both fusiform (patients AAA₁, AAA₇), single balloon shaped (patients AAA₄, AAA₅, AAA₁₀, AAA₁₁), and bi-lobbed aneurysms (patients AAA₃, AAA₆, AAA₈, AAA₉). We consider geometries featuring straight necks (patients AAA₁, AAA₄, AAA₅, AAA₈), and more angulated necks (patients AAA₃, AAA₇, AAA₉, AAA₁₀, AAA₁₁).

We can also differentiate among AAA cases based on the lumen size. With this purpose we define the radius R as the distance of each point of the lumen surface from the centerline, i.e., it is roughly half of the diameter. Both centerline and R are automatically computed during the segmentation procedure. R is also used as color map scale in Figure 3 to allow the reader understand the relative size of the different aneurysms. Considering that in case of thin ILT the dimensions of the lumen approximately corresponds to the dimensions of the aneurysm and recalling the critical diameter value of 55 mm (≈ 27.5 mm in terms of distance from centerline), we consider at risk AAA₁₀ and AAA₁₁. Near a critical value there are AAA₁, AAA₄, AAA₅, AAA₉ aneurysms, while AAA₃, AAA₇ and AAA₈ cases are at a lower risk. The case of AAA₂ seems to be far from a critical situation both in terms of shape and diameter measurements.

Age	Sex	AP AAA	LL AAA	Morphology	AP Neck	LL Neck	BMI	Calcifications
76	M	40mm	42mm	Aortic	20mm	20mm	22	Mild
80	M	35mm	35mm	Aortic	22mm	22mm	27	Mild
79	M	51mm	40mm	Aortic	22mm	22mm	23	Severe
86	M	44mm	45mm	Aortic	19mm	19mm	25	Mild
91	M	50mm	51mm	Aortic	18mm	18mm	23	Mild
82	M	48mm	42mm	Aortic	20mm	22mm	27	Mild
78	M	46mm	40mm	Aortic	31mm	28mm	22	Intermediate
80	M	27mm	32mm	Aortic	18mm	18mm	28	Interm., with dissection
71	M	45mm	47mm	Aortic	18mm	18mm	33	Intermediate
77	M	57mm	54mm	Aortobiiliac	19mm	20mm	25	Mild
72	M	50mm	52mm	Aortic	19mm	19mm	25	Mild

Table 1: Patients demography and AAA morphological characteristics. AP: Antero-posterior radius R of the AAA and Neck, respectively; LL: Latero-lateral radius R of the AAA and Neck, respectively.

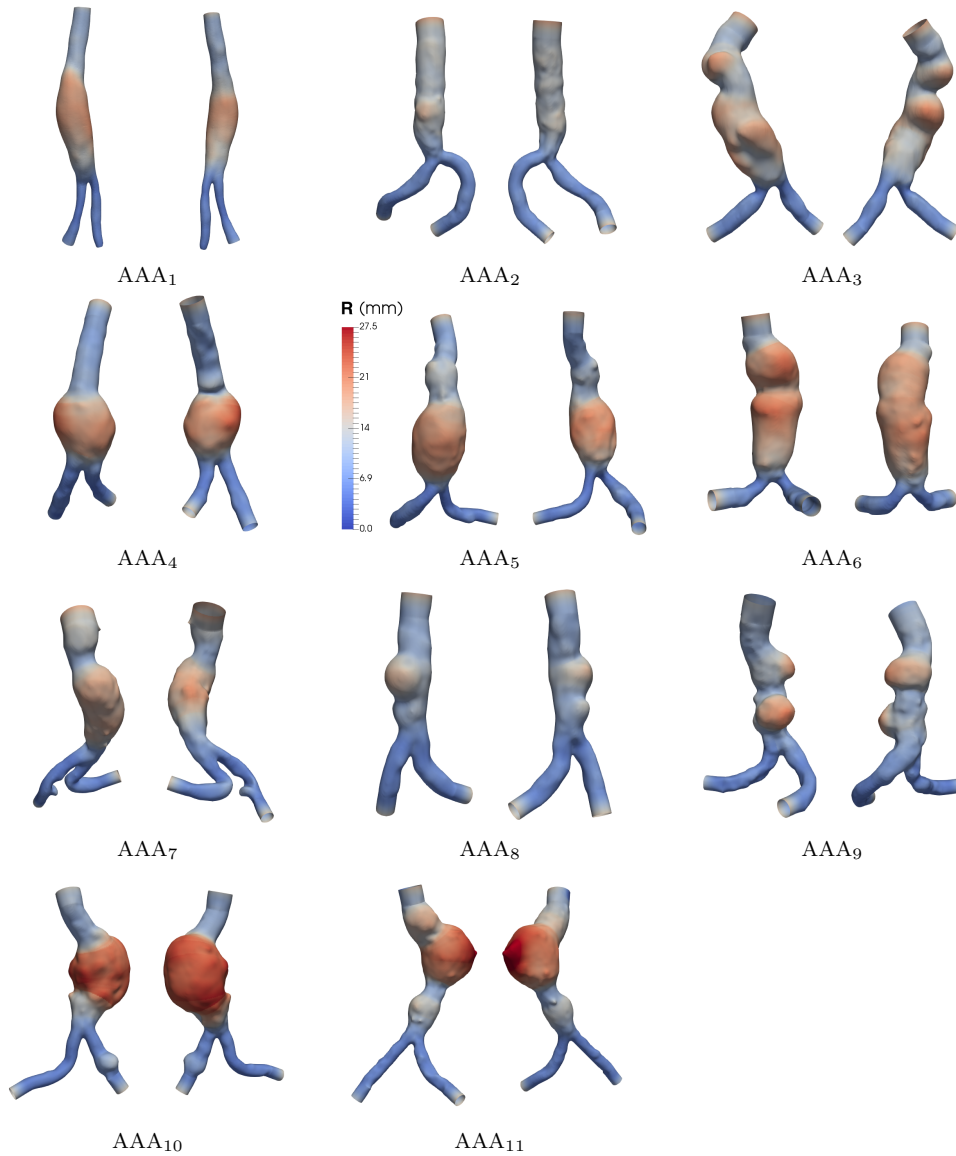


Fig. 3: Reconstructed lumen surfaces of eleven different abdominal aortic aneurysms. For each case, we display the results with two camera viewpoints. The color map shows the distribution of the R variable, i.e. the distance of each surface point from the centerline.

3 Haemodynamics model

3.1 Model equation

Blood is a heterogeneous media, composed by a particulate phase and a liquid one. Despite its heterogeneity, as a common assumption, blood in large vessels (diameter greater than roughly 0.3 cm, e.g. aorta) is considered as a continuous media since the dimension of the particles is of orders of magnitude smaller than the diameter of the vessel. The fluid in these vessels is incompressible, viscous and is modelled using the well-known Navier-Stokes equations (e.g. [38,27]). In large arteries, it is also widely accepted to assume blood as a Newtonian fluid and, thus, characterized by a constant viscosity [38]; for simplicity we assume that this hypothesis holds also in presence

of an AAA. Being $[0, T]$ the temporal interval of interest (typically, several full heartbeats) the Navier-Stokes system reads as follows:

$$\begin{cases} \rho_f \frac{\partial \mathbf{u}}{\partial t} + \rho_f (\mathbf{u} \cdot \nabla) \mathbf{u} - \nabla \cdot \boldsymbol{\sigma}_f = 0 & \text{in } \Omega \times [0, T], \\ \nabla \cdot \mathbf{u} = 0 & \text{in } \Omega \times [0, T] \end{cases} \quad (1)$$

where \mathbf{u} and p are the velocity and pressure of the blood, respectively, and ρ_f is its density (set equal to 1 g/cm³). We denote by $\boldsymbol{\sigma}_f$ the Cauchy stress tensor

$$\boldsymbol{\sigma}_f = \mu_f (\nabla \mathbf{u} + (\nabla \mathbf{u})^T) - p \mathbf{I},$$

with \mathbf{I} being the identity tensor and μ_f the blood dynamic viscosity (set equal to 0.04 Pa·s). We refer to Ω as the portion of the lumen wherein we are interested in simulating the blood flow. When considering haemodynamics problems in arteries, the domain Ω is indeed changing in time due to the vessel compliance. Nevertheless, since these variations are small, in a first approximation, we may assume as fixed the domain Ω . We remark that completely neglecting the presence of the compliant tissue may heavily affect the resulting pressure wave or the values of the wall shear stress, as it happens in rigid wall models. Thus, while keeping Ω fixed, to mimic the effect of the surrounding material, we introduce a non-rigid boundary condition on the lateral surface of the lumen. The condition is derived by a three dimensional linear isotropic elastic model condensed as a two dimensional membrane [23,13]. The resulting condition on the lateral surface of the lumen depends on the mechanical properties assigned to the vessel wall. In particular, we set the vessel's Young modulus equal to 10⁷ dyn/cm², the Poisson's ratio equal to 0.5, and we suppose a constant vessel thickness equal to 1.5 mm.

To close the physical model, we need to specify boundary conditions at the inlet and outlet surfaces. In particular, at the outlets, we aim at imposing a mean pressure value. We prescribe the values \tilde{P}_{right} and \tilde{P}_{left} of the pressures at the right and left iliac, respectively, using the absorbing boundary condition formula as proposed in [39]. At a given time step the value of \tilde{P}_{right} (and, similarly, \tilde{P}_{left}) is determined by an algebraic formula depending on the values of the flowrates, pressures and areas at previous time steps computed on the corresponding iliac section. To avoid numerical instabilities and the occurrence of non-physical flows from one iliac to the other, we further assume that both iliac arteries are at the same pressure level. We average the values \tilde{P}_{right} and \tilde{P}_{left} obtaining our final outlet mean pressure condition $P_{\text{out}} = 0.5(\tilde{P}_{\text{left}} + \tilde{P}_{\text{right}})$ that we impose at both the iliac arteries.

At the inlet surface we impose a mean population flowrate as proposed in [33] (see Figure 4) and we choose a Poiseuille velocity profile. As we explain later, the inlet is extended upstream such that it is possible to exactly impose this profile.

3.2 Numerical approximation

The solution of problem (1) is approximated by means of the Finite Element Method (FEM). We generate unstructured *meshes* using tetrahedral elements [42,43] and we add a thin layer of elements on the lateral boundary to increase the accuracy near the vessel wall (see Fig.5) [7]. We add cylindrical extensions at each inlet/outlet surface in order to lower the dependency of the results in the aneurysm's sac from the chosen boundary conditions. As for the segmentation, also the FEM mesh generation is performed by automatic algorithms [20,21]. The inlet was selected right below the renal bifurcation. Going higher would have required to take into account and segment the renal arteries which is a quite challenging process to automatize. The results depend on the boundary conditions and the extension were added to be able to ease the imposition of the inlet flowrate on a circular inlet surface. To assess the effect of these assumptions, comparisons with patient-specific boundary conditions should be performed. Unfortunately, patient-specific inlet data were not available.

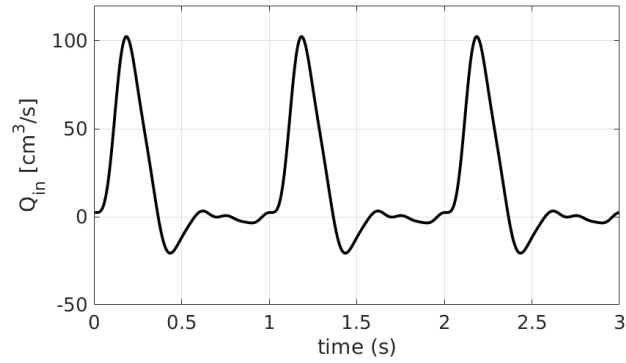


Fig. 4: Flow rate inlet wave at rest conditions imposed at the inlet section for all AAA cases (three heartbeats).

System (1) is then solved using P1-P1 discretization with bubble functions stabilization in space and a second order backward difference formula in time. The interested reader can find more details about these techniques in, e.g., [43]. The dimension of the system of equations to be solved for each AAA is of order of millions (between 4 and 7 millions). The time step is fixed to $\Delta t = 0.001$ seconds yielding 1000 solver calls per heartbeat. Since these discretisation parameters are quite fine for this kind of situation, we did not perform specific convergence studies. To compute the target indexes, we process simulation results belonging to the fourth heartbeat, in order to get rid of the dependency of the initial conditions. We sample and store the solutions every 5 time steps (every 0.005 s) resulting in 200 time instances for each AAA case. We compute the time integral in the TAWSS's and OSI's formulas (cf Section 4.1) using trapezoidal numerical integration rule.

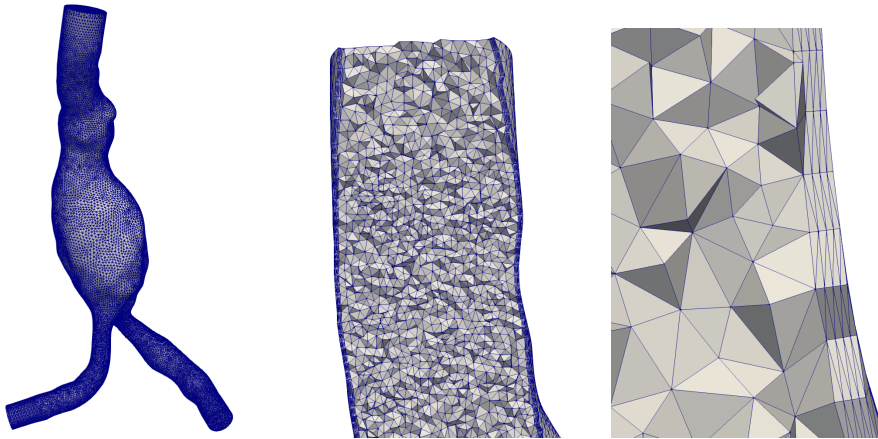


Fig. 5: Example of finite element tetrahedral mesh with boundary element layer on the lateral surface. On the center and on the left, zoom of the computational mesh to visualize the boundary layer near the lateral surface.

4 Index computation

4.1 Wall Shear Stress

Our comparisons are focused on two haemodynamical outputs computed on the lumen lateral surface.

- Time Averaged Wall Shear Stress (TAWSS). Wall Shear Stress (\mathbf{wss}) are defined by the tangential component of the traction vector, i.e

$$\mathbf{wss} = \boldsymbol{\sigma}_f \mathbf{n} - ((\boldsymbol{\sigma}_f \mathbf{n}) \cdot \mathbf{n}) \mathbf{n}, \quad (2)$$

where \mathbf{n} is the normal outward unit vector to the lumen surface. WSS is a vectorial quantity and TAWSS is the time averaged, over a period of one heartbeat, of its magnitude:

$$\text{TAWSS} = \frac{1}{T} \int_{t_0}^{t_0+T} |\mathbf{wss}| d\tau. \quad (3)$$

TAWSS is an indicator of the averaged shear stress to which the luminal surface is subjected. The notation $|\mathbf{wss}|$ indicates the Euclidean norm of the vector \mathbf{wss} measured in dyn/cm^2 .

- Oscillatory Shear Index (OSI). When observing WSS, it is not only important to compute its magnitude but also to keep track of its direction changes. OSI is defined as follows:

$$\text{OSI} = 0.5 - 0.5 \frac{\frac{1}{T} \left| \int_{t_0}^{t_0+T} \mathbf{wss} d\tau \right|}{\text{TAWSS}}. \quad (4)$$

Unidirectional flows yield a low value of OSI, while highly oscillating flows are characterized by OSI near 0.5.

4.2 MFA-ILT

We would like to provide evidence that haemodynamical indexes can be used as first level indicator of ILT deposition risk. With this purpose, we need to measure an ILT deposition index from the medical images resulted from the CT-scan. Precisely, we aim at locating those regions where the ILT has started to deposit. We assume that the areas, where we currently observe a thin ILT layer, coincide with areas at high risk of deposition and, thus, where the ILT will continue to grow. To perform quantitative comparisons, the MFA-ILT is reconstructed directly on the lumen surface, where also the haemodynamical indexes will be computed. Upon reading and properly processing the information contained in the DICOM images, at each point of the lumen we assign a scalar value measuring the level of MFA-ILT that has been deposited around the point itself.

In DICOM images, each pixel, representing a physical point, is colored using a gray scale color map. The contrast liquid makes blood appear in a bright color. We probe the minimum and maximum values (namely, v_{min} and v_{max}) of the gray scale associated to the MFA-ILT directly from the DICOM images. For AAA_i with $i = 1, \dots, 8$, v_{min} is equal to 0 and v_{max} to 200. For AAA_i with $i = 9, 10, 11$, v_{min} is equal to 1000 and v_{max} to 1200.

The MFA-ILT deposition index is computed by performing the following three steps:

1. *Mask*. Other tissues different from ILT are associated with the same gray scale values. This is the case, for example, of the blood flowing inside the *vena cava*, located close to the abdominal aorta. These structures may affect the computation of MFA-ILT, detecting a misleading presence of ILT where indeed there is no deposition. Thus, the first step of the image processing is the application of a *mask* to these components: we enclosed the target structures using several volume spheres and we blacken all the pixel laying inside the spheres. This step is difficult to automatize and is performed manually. An example of this process on a single DICOM slice is shown in Figure 6.

2. *Filtering.* Denoting by y the scalar gray scale value we define $\lambda(y)$ as follows:

$$\lambda(y) = \begin{cases} 0 & \text{if } y < v_{min} \\ 1 & \text{if } v_{min} \leq y \leq v_{max} \\ 0 & \text{if } y > v_{max} \end{cases}$$

As result of the *filtering*, the MFA-ILT (and, also the other structure with a similar gray scale) are visualized in white while all the rest is blackened. An example is shown in Figure 7-(b).

3. *Averaging.* At each point $\bar{\mathbf{x}}$ of the lumen surface we consider the sphere $S_{\bar{\mathbf{x}}}$ of radius 8 mm centered in $\bar{\mathbf{x}}$ and we average λ on all the pixel lying inside this sphere. The formula of the MFA-ILT index reads as follows:

$$\text{MFA-ILT}(\bar{\mathbf{x}}) = \frac{\sum_{\mathbf{x}_i \in S_{\bar{\mathbf{x}}}} \lambda(y(\mathbf{x}_i))}{N}, \quad (5)$$

where N is the total number of points \mathbf{x}_i lying inside the sphere $S_{\bar{\mathbf{x}}}$. In Figure 7-(c), we show an example of the sphere $S_{\bar{\mathbf{x}}}$ (in yellow) around the point $\bar{\mathbf{x}}$ (in pink). We choose a sphere of radius 8 mm such that MFA-ILT is not affected by the arterial wall layer (1.5-2.5 mm of thickness). Being the sphere centered on a surface lumen point and being the internal part of the lumen filled with blood, we expect that the thrombus deposition is characterized by MFA-ILT values greater than 0.3, with maximum values around 0.5-0.6 (depending on the surface curvature). The threshold of 0.3 is also confirmed by visual assessment, as shown in Figure 8

In Figure 8 we display the resulting MFA-ILT index on a section of the lumen surface for the case of AAA5.

Remark 1 The values v_{max} and v_{min} have been selected by probing the gray levels of the ILT and of the lumen. Consistent values were found in all the DICOM files and for all the patients. Small variation of these numbers of order of units do not change the results.

The range of thickness of CTA ranges from 0.625 to 2.0 mm, cf Table XX, although in our protocol thickness used for aortic imaging is 1.0 mm. Computational Tomographic Angiography (CTA) scan were obtained from real-world patients that should be submitted to open or endovascular aortic repair (EVAR) at Policlinico di Milano. In many cases, it was already available at admission. So, for ethical reasons (exposure to radiation, nephrotoxic and allergic risks) we have avoided to repeat CTA and we have used the available imaging to perform the study.

AAA ₁	AAA ₂	AAA ₃	AAA ₄	AAA ₅	AAA ₆	AAA ₇	AAA ₈	AAA ₉	AAA ₁₀	AAA ₁₁
1.25	1.5	2.0	1.0	2.0	0.625	2.0	2.0	2.0	1.5	1.0

Table 2: Thickness of the CTA in mm for the different patients.

Remark 2 The radius of the sphere for averaging the filtered values has been chosen equal to 8mm. Going lower than 8mm is not sustainable because of the arterial layer. Values 8mm-10mm allow to retrieve qualitative good results. We should also keep in mind that the result depend from the *Mask* step, which is manual. Considering a larger sphere is also affecting negatively the results because of the presence of these tissue that it was not possible to mask perfectly.

5 Comparison of the indices

The pre-processing of the numerical simulations, comprising geometry reconstruction and mesh generation, was performed using *semi-automatic segmentation* algorithm of the aXurge platform [20]. The computation of the MFA-ILT was performed using VMTK library [3] and Matlab [36] software. The numerical simulations were performed using the LifeV [8] finite element library

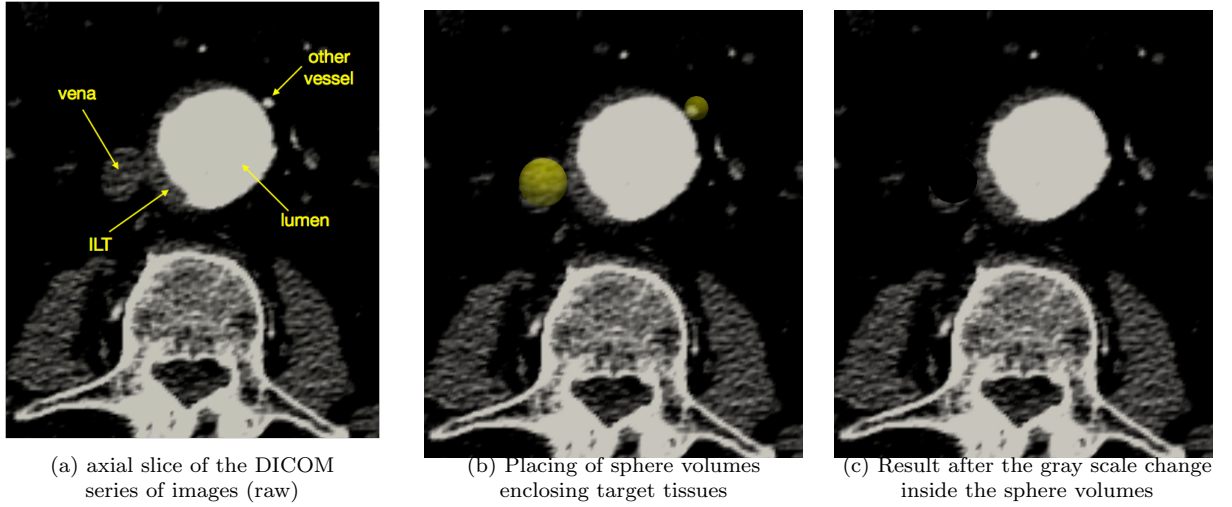


Fig. 6: Example of *cleaning* process of the DICOM images.

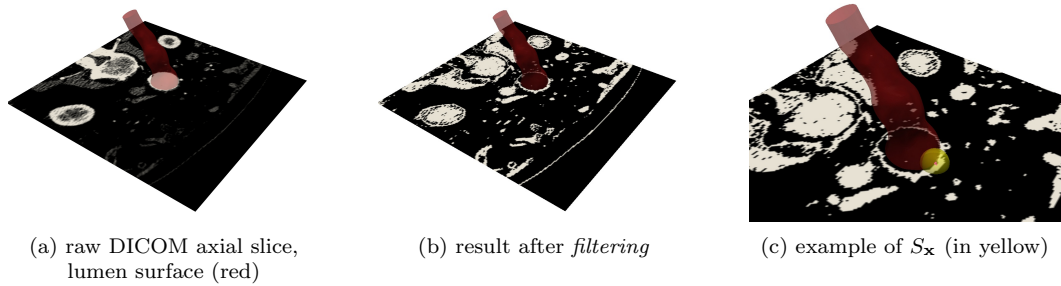


Fig. 7: Example of the *filtering* image processing step and of the construction of S_x for the *averaging* image processing step.

and using resources of the Swiss SuperComputing Center (Lugano). The post processing and the computation of the indexes were performed using Paraview [6] and Matlab [36] software.

We compare the MFA-ILT, haemodynamics and morphological indexes only on the aneurysm region, thus excluding the aorta neck and the iliac branches. We recall that we compute the indexes in correspondence of all the vertices of the surface finite element meshes. TAWSS and OSI are properly derived from the surface normal fields and the velocity field obtained by numerical simulations. The numerical simulations provide the velocity field and pressure (1). In the post-processing of the results, TAWSS and OSI are derived from the velocity field using equations (2), (3), and (4), where the surface normal field has been computed using Paraview [6]. To reduce local effects of sudden changes in the normal field, we average in space TAWSS and OSI on a small sphere of radius 2 mm centered in each surface vertex. To simplify the discussion of the result we address the inverse of TAWSS ($= \text{TAWSS}^{-1}$) with invTAWSS .

In Figure 9 we plot the values of the invTAWSS versus the MFA-ILT ones. Each one of red points in Figure 9 represents a vertex of the surface mesh. We aim at testing a linear regression model between invTAWSS and MFA-ILT. We normalize both MFA-ILT and invTAWSS with respect to the maximum values attained in each specific AAA case:

$$\overline{\text{invTAWSS}}_i = \frac{\text{invTAWSS}_i}{\max(\text{invTAWSS}_i)} \quad \overline{\text{MFA-ILT}}_i = \frac{\text{MFA-ILT}_i}{\max(\text{MFA-ILT}_i)} \quad \forall \text{AAA}_i, i = 1, \dots, 9.$$

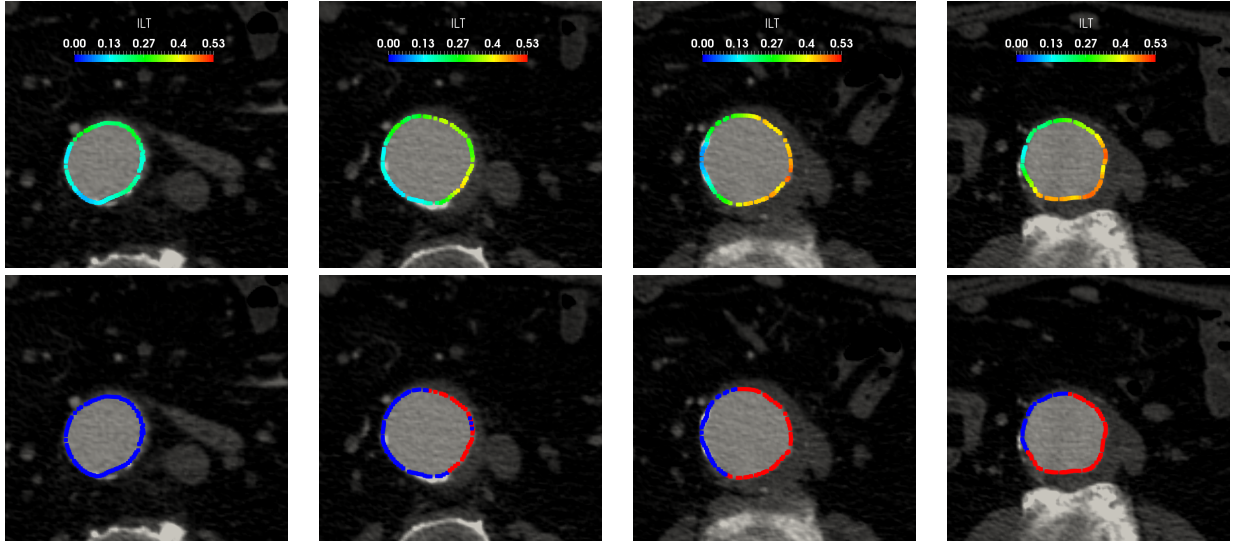


Fig. 8: Results of the MFA-ILT computation on 3 axial slices of the DICOM series of images. Lower row: in red MFA-ILT > 0.3; in blue, MFA-ILT < 0.3

Name	m_i	SE	R-squared	pValue
AAA ₁	3.0108	0.1121	0.0896	< 0.005
AAA ₂	2.7810	0.1237	0.0657	< 0.005
AAA ₃	8.5778	0.3483	0.0593	< 0.005
AAA ₄	3.9467	0.1050	0.1997	< 0.005
AAA ₅	19.3618	0.2176	0.5040	< 0.005
AAA ₆	3.2999	0.1272	0.0817	< 0.005
AAA ₇	2.9039	0.2171	0.0258	< 0.005
AAA ₈	2.1494	0.1020	0.0927	< 0.005
AAA ₉	5.7224	0.0932	0.3940	< 0.005
AAA ₁₀	2.8966	0.3542	0.0096	< 0.005
AAA ₁₁	10.5039	0.1902	0.2608	< 0.005

Table 3: Results of the linear regression model between invTAWSS and MFA-ILT.

Note that these choices have an influence on the m coefficient. Then, we test the following model

$$\overline{\text{TAWSS}}_i^{-1} = m_i \overline{\text{MFA-ILT}}_i + q_i \quad \forall \text{AAA}_i, i = 1, \dots, 9. \quad (6)$$

The estimates of m_i , the corresponding Standard Errors (SE) and the p-value for the t-statistics are reported in Table 3.

From the results, we notice that low level of invTAWSS (and thus high TAWSS) are linked with low MFA-ILT. Linear regression models give positive angular coefficients in all the cases. We notice that among 11 aneurysm cases, 5 of them (AAA₁, AAA₂, AAA₆, AAA₇, AAA₁₁) show a m_i coefficient around 3. Other cases show much higher m_1 coefficients ($m_5 = 19.362$ or $m_{10} = 10.504$). It is not likely to derive an absolute coefficient that is suitable for all the cases.

From the results of Figure 9, we aim at studying if invTAWSS can be used as a preliminary indicator of ILT deposition. To support this hypothesis, we aim at checking if a clustering algorithm on these data-sets automatically detects two regions: the first one featuring high values of invTAWSS and high values of MFA-ILT; the second one characterized by low values of invTAWSS and, as well, low values of MFA-ILT. From the clustering results, we aim at further verifying if it is possible to define a threshold value of invTAWSS that can be used to detect the region at high/low risk of ILT deposition. Graphically, this threshold would correspond to a horizontal clustering separation among the points in Figures 9.

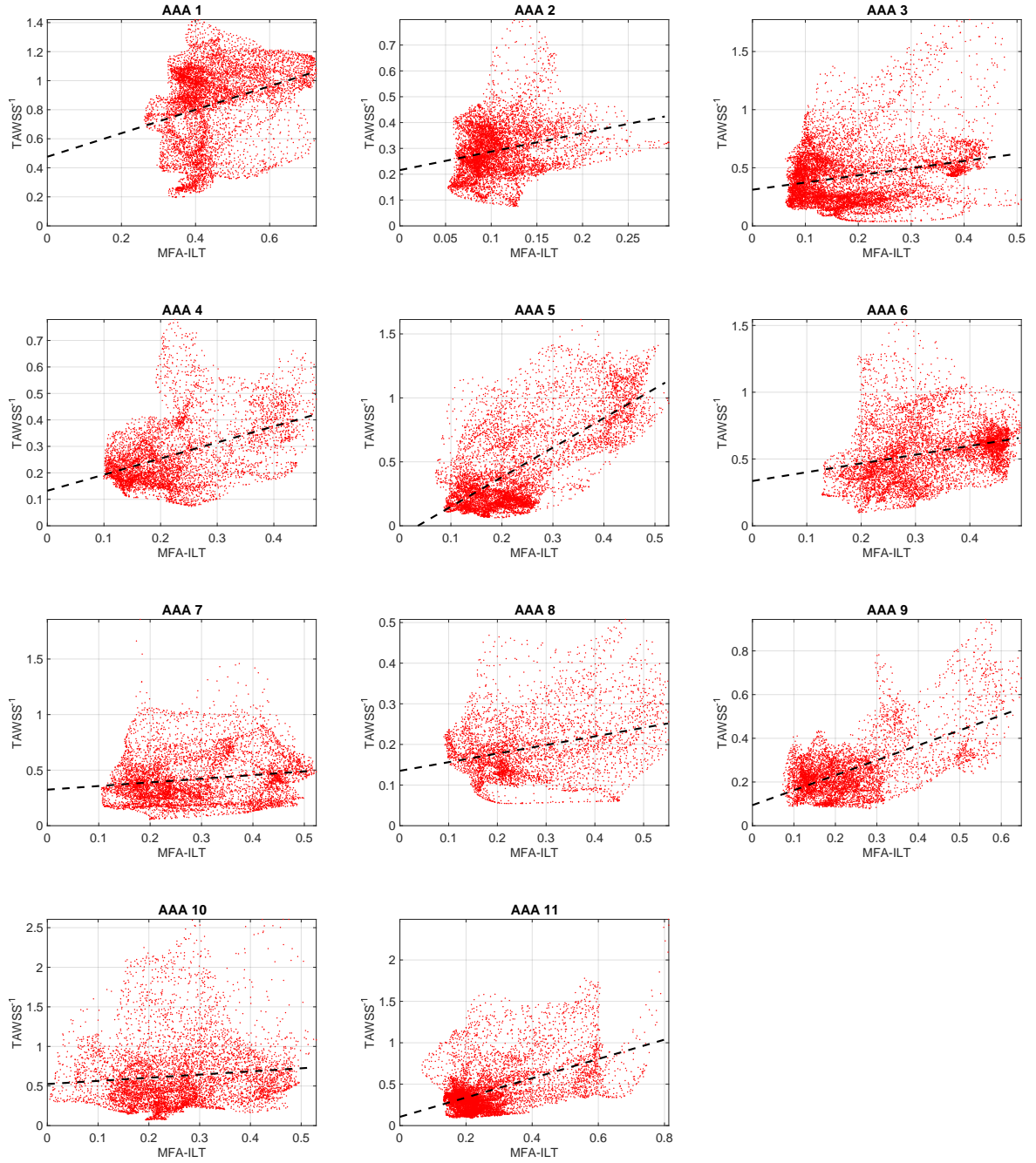


Fig. 9: invTAWSS vs MFA-ILT . In black: linear regression straight line.

We recall from section 4.2 that the deposition of thrombus is associated to MFA-ILT values greater than, roughly, 0.3. We exclude indeed from the clustering analysis both AAA_1 and AAA_2 cases: the former presenting too high values of MFA-ILT in all the points (> 0.3) and the latter featuring too low MFA-ILT values all over the lumen surface (< 0.3). The number of cluster was chosen a-priori equal to two and the exact command which is used for the clustering algorithm is

```
opts = statset('Display','final');
```

Name	MFA-ILT red cluster	MFA-ILT blue cluster	invTAWSS red cluster	invTAWSS blue cluster
AAA ₃	0.1737	0.1549	0.561	0.2401
AAA ₄	0.3255	0.177	0.4009	0.1983
AAA ₅	0.3723	0.1813	0.861	0.2231
AAA ₆	0.4049	0.2569	0.6497	0.37
AAA ₇	0.3512	0.2341	0.6103	0.2851
AAA ₈	0.3982	0.1999	0.2278	0.1614
AAA ₉	0.4641	0.1853	0.438	0.2075
AAA ₁₀	0.2768	0.2306	0.8888	0.3819
AAA ₁₁	0.4179	0.2111	0.7993	0.3033

Table 4: MFA-ILT and invTAWSS values at the centroids of the red and blue clusters in Figures 10.

```
kmeans(X',2,'Distance','city','Start','cluster','Replicates',20,'Options',opts);
```

We run a k-means algorithm on AAA_{*i*} for $i = 3, \dots, 11$. We color the points of each aneurysm data set depending on the results of the cluster algorithm: the points whose centroid has the highest MFA-ILT value are represented in red and in blue the points referring to the other cluster (see Figure 10). We notice that in six cases (namely AAA₄, AAA₅, AAA₆, AAA₇, AAA₉, AAA₁₁), out of the nine considered here, the clustering algorithm produces the expected result: the centroids are aligned along the principal diagonal of the x-y plane, allowing us to detect two populations: the blue one characterized by low MFA-ILT and low invTAWSS and the red one featuring high MFA-ILT and high invTAWSS. Moreover, for each one of these six aneurysms, the separation between the two clusters is roughly horizontal; this allows us to define the threshold value for invTAWSS such to differentiate between the areas at low and high risk of ILT deposition. For these six cases, we remark that all the centroids of the red clusters are characterized by an MFA-ILT value above 0.3 and the correspondent values for the blue clusters are around 0.2 (see Table 4). This result confirm that the visual assessment of 0.3 as a discriminant for the presence of ILT. On the other side, concerning the values of invTAWSS, it is not possible to define a value that can be used as an absolute threshold for all the AAA cases. In particular, we note that the invTAWSS characterizing the centroid of the blue cluster of AAA₁₁ are closed to the centroids' invTAWSS values of the red clusters of AAA₄ and AAA₉. The clustering results obtained in the case of AAA₃ and AAA₁₀ are not satisfactory since the two centroids are almost vertically aligned, meaning that the two clusters are characterized by the same averaged value of MFA-ILT deposition index. The results are not as expected also in the case of AAA₈: despite the fact that the centroids are aligned on the principal diagonal, the cluster separation is vertical, which means that invTAWSS cannot indeed be used as a discriminant factor to detect ILT deposition areas.

We aim at further studying if through the solely information of invTAWSS, we can detect the aneurysm region at high risk of ILT deposition. Using the centroids obtained from the cluster analysis, we compute two thresholds, one for MFA-ILT and another for invTAWSS, averaging the centroids' coordinates. These thresholds are reported in Figure 11. We notice that, as expected, all the MFA-ILT thresholds are around 0.3. The minimum MFA-ILT threshold is 0.25125 obtained for AAA₄ and the maximum is 0.3309 obtained for AAA₆. We use the MFA-ILT and invTAWSS thresholds to construct a visual comparison on the six aneurysms on which the cluster algorithm produced satisfactory results. In Figure 11, for each aneurysm we show four pictures: on the left we have two viewpoints of the three-dimensional regions determined by the invTAWSS threshold and on the right we show two viewpoints of the three-dimensional regions determined by the MFA-ILT threshold. In red we color the points above the thresholds, in blue the points below. The pattern obtained using the invTAWSS threshold is highly correlated with the ones obtained with the threshold of the MFA-ILT index. Once again, we remark that it is not possible to identify an absolute threshold for the invTAWSS suitable for all the AAA cases due to the high variance of this values among the six aneurysm cases (from 0.29955 for AAA₄ to 0.54205 for AAA₅). Further investigations with bigger samples would be needed to identify an a-priori threshold of the invTAWSS that can be used to infer the region at high risk of ILT deposition. In Figure 12 we show the pattern comparisons in the three cases where the cluster algorithm failed.

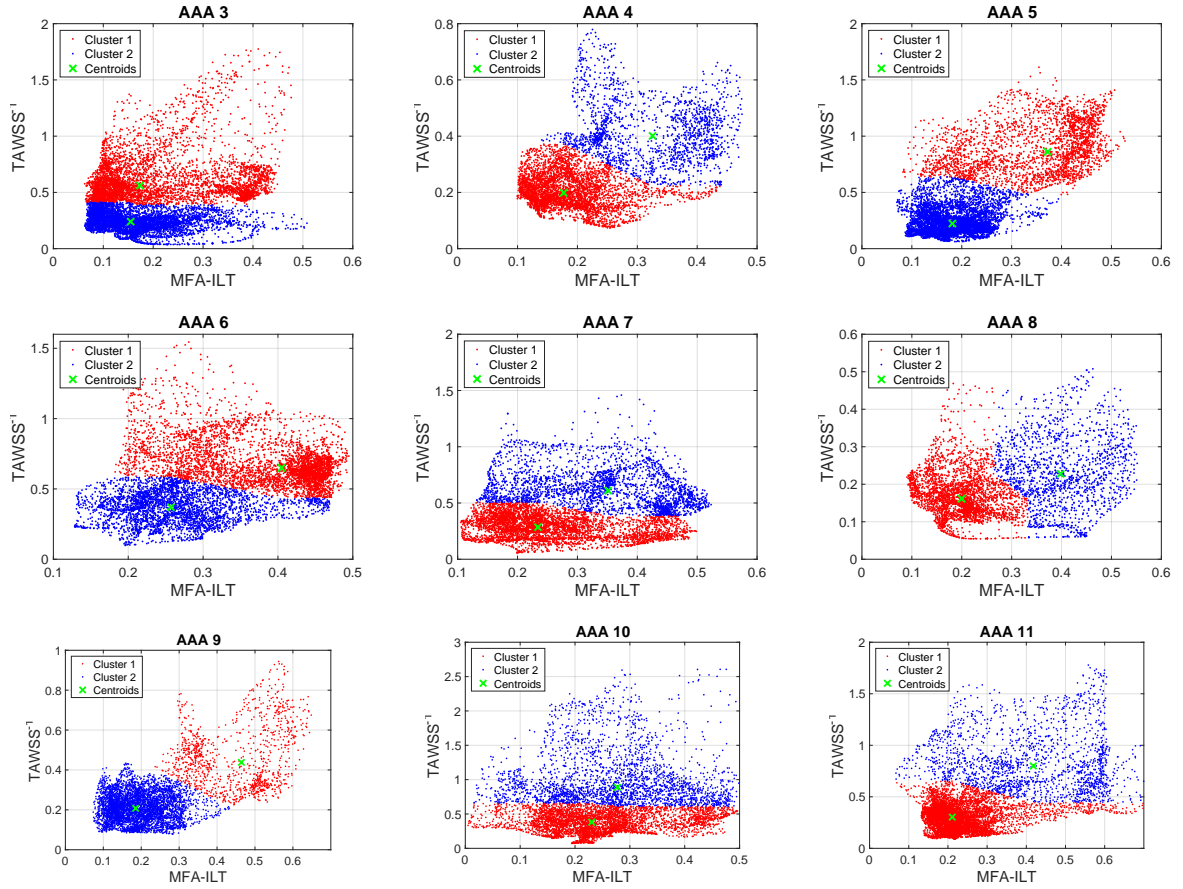


Fig. 10: K-means clustering results.

In Figure 13 we display the distance from centerline, R , versus MFA-ILT in each vertex of the aneurysm surface mesh. In Table 5 we also report the regression results. The results are not very different from those in Table 3 about invTAWSS . Indeed, the diameter is the current index that it is used in the clinical setting to assess abdominal aortic aneurysms. However we do believe that the hemodynamical indices contribute to better evaluate the clinical situation. We do not observe any strong correlation between R and MFA-ILT index. In particular, at low values of MFA-ILT corresponds both low and high R values.

Finally, in Figure 14 we display the MFA-ILT index versus the OSI in each vertex of the aneurysm surface mesh. In this case, we do not test linear regression model, since any strong relation between the two variables can be seen from our data. This is in contrast with what is reported in literature (e.g. [17]), where oscillatory shear stresses are typically correlated with re-circulation and deposition of thrombi. We recall that our models are based on several assumptions and, in particular, we used the same inflow boundary conditions for all the different AAA cases. The relation between OSI and MFA-ILT should be further investigated when patient-specific flow conditions are available.

6 Conclusions

The aim of this work is to investigate the correlation between haemodynamical indexes with measured data about the deposition of ILT. We considered eleven different geometries of both

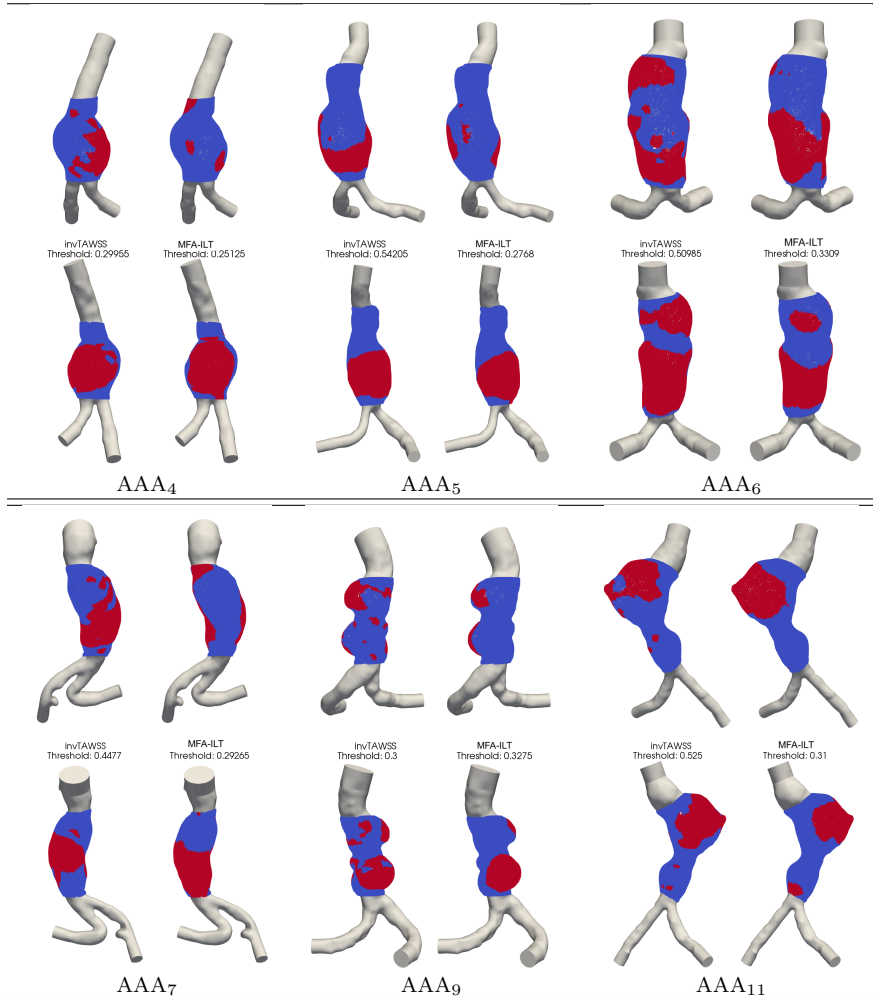


Fig. 11: TAWSS vs MFA-ILT.

Name	m_i	SE	R-squared	pValue
AAA ₁	0.3264	0.0117	0.0965	< 0.005
AAA ₂	0.1822	0.0092	0.0522	< 0.005
AAA ₃	0.0662	0.0065	0.0106	< 0.005
AAA ₄	0.2440	0.0120	0.0683	< 0.005
AAA ₅	0.4379	0.0083	0.2620	< 0.005
AAA ₆	0.0348	0.0056	0.0050	< 0.005
AAA ₇	-0.0986	0.0079	0.0223	< 0.005
AAA ₈	0.2034	0.0085	0.1175	< 0.005
AAA ₉	0.5133	0.0059	0.5625	< 0.005
AAA ₁₀	0.0008	0.0120	-0.0002	0.94359
AAA ₁₁	0.7315	0.0076	0.5178	< 0.005

Table 5: Results of the linear regression model between R and MFA-ILT.

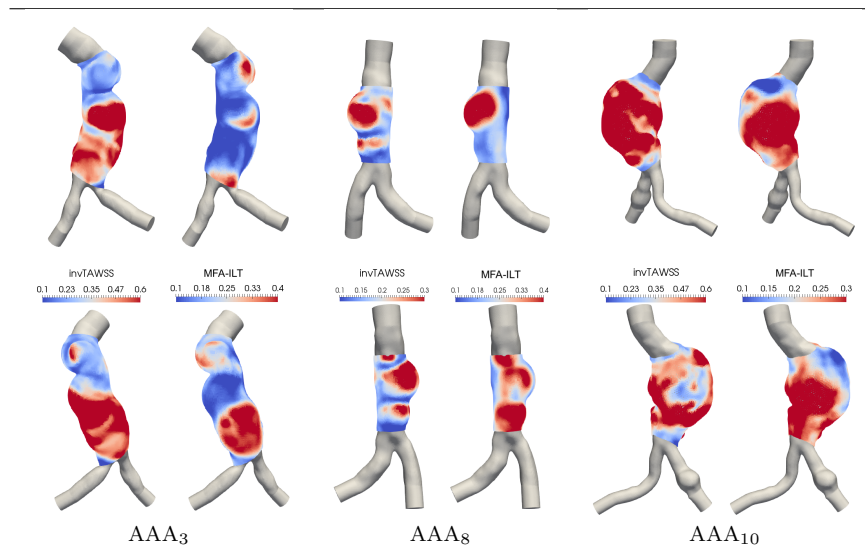


Fig. 12: TAWSS vs MFA-ILT.

developed and non-developed aneurysms, all showing a thin layer of ILT. Thanks to this thinness, we assume that the lumen geometry we currently observe from the DICOM images is not significantly different from the geometry before the ILT deposition. We also assume that the locations where we currently register a deposition of thin ILT correspond to areas at high risk of further deposition.

We have set up a three dimensional numerical model for eleven AAA cases, in particular we reconstruct the patient-specific geometries using automatic algorithms for segmenting and sizing. Thanks to these algorithms we are also able to automatically extract information about the distance of each lumen point from the centerline. We develop an image processing algorithm allowing us to measure the MFA-ILT projected on the luminal surface. We close the numerical model using mechanical parameters and boundary conditions coming from the corresponding literature and averaged population data. Our results show that there is a stronger correlation between invTAWSS (the inverse of TAWSS) and MFA-ILT rather than between R (distance to centerline) or OSI and MFA-ILT. This correlation should be further investigated and might be improved when further patient-specific data, e.g. flowrates and/or resistance coefficients, are available.

The role of WSS in AAA's growth has been already studied in literature, although the conclusions are not always agreeing. Di Martino et al [35] suggested that ILT could be protective against rupture. Aortic wall hypoxia has been postulated in regions of high ILT deposition, suggesting a mechanism for aortic wall expansion and degeneration [50], because ILT inhibits vascular smooth muscle cell synthesis of collagen, and has greater numbers of macrophages and inflammatory cells. Although not directly related to cause aortic rupture, continued deposition of ILT, and consequently of low WSS, could promote local biological reactions, such as ischemic changes or loss of adventitial integrity through inflammatory [32] and [51]. Regardless of aneurysm size or configuration, Boyd et al [10] reported that often rupture occurred in or near the zones of flow re-circulation, where WSS was significantly lower and thrombus deposition was more abundant. In our analysis, on the contrary, we notice that low level of invTAWSS (and thus high TAWSS) are linked with low MFA-ILT. AAA growth and rupture is multi factorial, with many factors still to be identified, but with pressure and local haemodynamics probably playing a significant role in the process of AAA's expansion.

We remark that invTAWSS and MFA-ILT indexes are computed using different algorithms: the first results from numerical simulations, while the second is directly measured from DICOM data using image processing techniques. We also remark that invTAWSS has been reconstructed

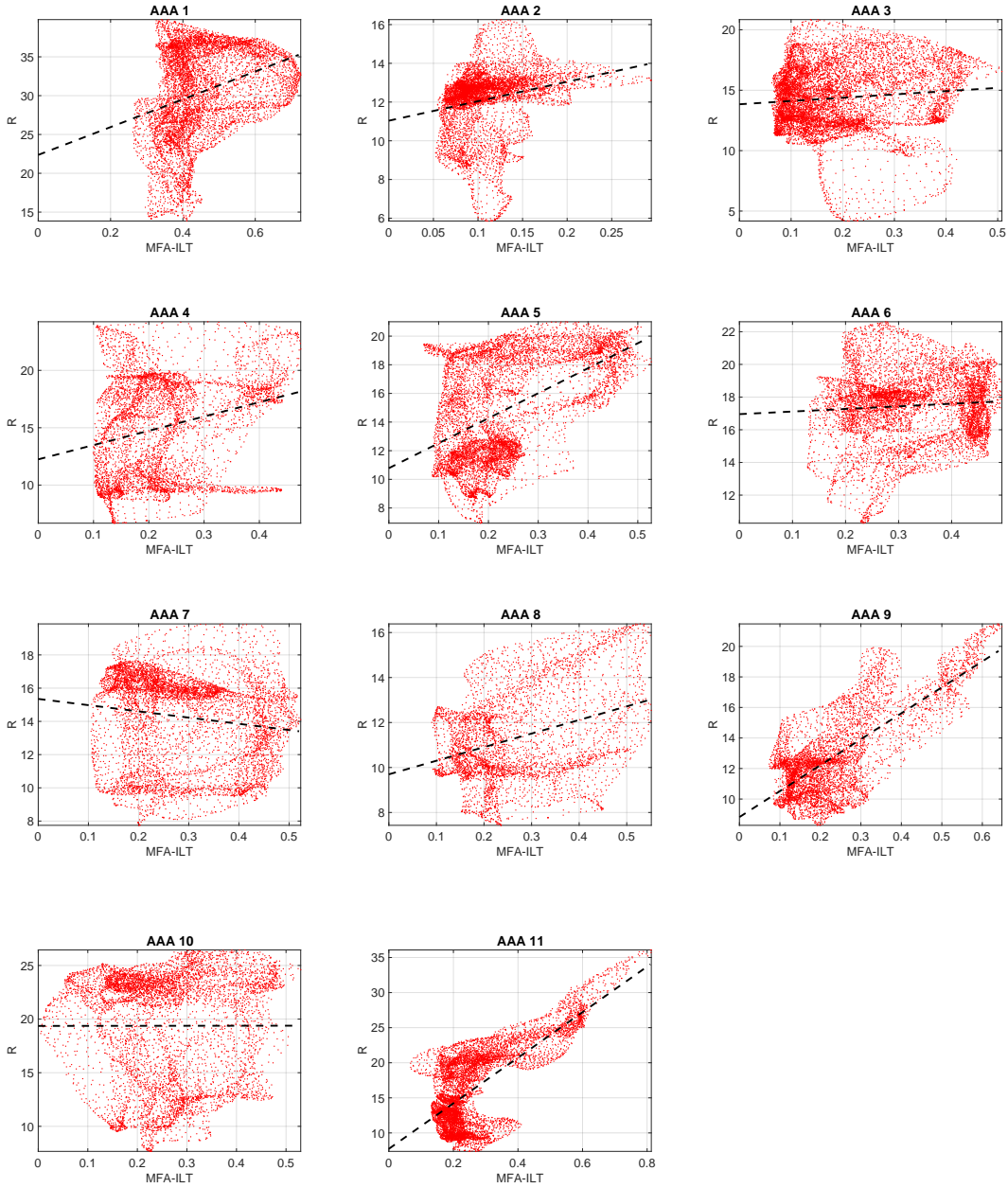


Fig. 13: Distance from centerline R vs MFA-ILT.

with a minimal interaction from an external user: the data required for the computation of this index are indeed the DICOM data and the input five points required to initialize the segmentation algorithm. The only shared information between the indexes is the geometry and, thus, the points of the lumen surface where they are computed. The comparisons have been carried on different morphological AAA cases and, in the majority of the cases, we notice a correlation between the value of invTAWSS and MFA-ILT. In particular, low values of invTAWSS yield low values of MFA-ILT. In some AAA cases, we also observe that high values of invTAWSS are linked with high values of MFA-ILT. This consideration is also supported by the results of the cluster analysis which, in six cases out of nine, allows us to separate the lumen surface in two areas, the first one

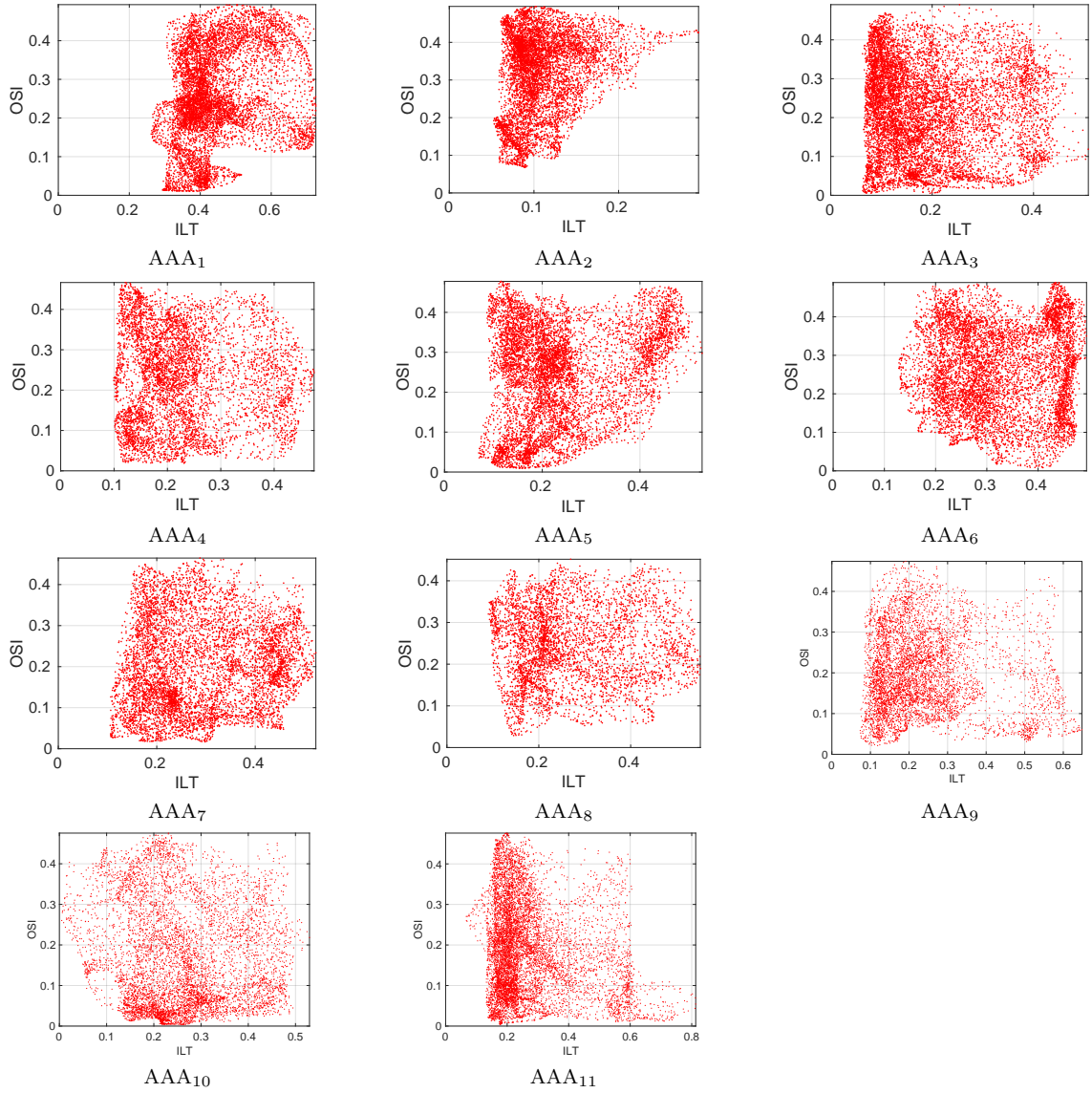


Fig. 14: OSI vs MFA-ILT.

characterized by low invTAWSS and low MFA-ILT and the second one by high invTAWSS and high MFA-ILT. The clustering allows us to detect invTAWSS threshold values that can be used as predictor for regions at high risk of ILT deposition.

Limitations and further studies. Among the limitations of our method, we recall that the thresholds above are relative to each single aneurysm case and from our data it was not possible to determine an absolute threshold of the invTAWSS values. There is some degree of arbitrariness both in the threshold definition and in the choice of the sphere radius. Unfortunately, at the best of our knowledge, there is no certified method to segment the ILT to compare with and to validate our results. The best comparison we can perform is a qualitative assessment with a medical expert eye, who has identified the 0.3 threshold, cf. also Figure 8. It is also worth to note that the MFA-ILT index does not correspond to any physical quantity and it is supposed to be read in comparative terms and not in absolute ones. We note also that the clusters do not appear very well separated.

The R-squared values are quite far from 1 actually, hence caution is needed when representing the variability of the indices with the regression models.

The physical models consider simple fluid and vessel laws, namely a Newtonian fluid and a linear isotropic material with constant parameter values. The influence of these choices on the indexes has not been investigated. The same holds for the inlet and outlet boundary conditions, including the cylindrical extrapolation of the geometry. Further studies are necessary to understand if better choices on the model can lead to better correlations between the indices or the development of ILT.

Further data should be collected on a larger AAA sample and, in particular, validation might be achieved using more patient-specific input data. The same methodology can be replicated also when *evolutive* AAA cases are available to provide further evidence of the utility of haemodynamical indicators. If patient-specific data are not available, our results show that numerical simulations, even with averaged population input data, provide better indicators than the sole distance from centerline. Haemodynamical indexes might be introduced, in cases of early stage AAA, to provide support to clinicians' decisions as they provide a preliminary indicator to identify those areas that are at low risk of ILT deposition.

Acknowledgments. We thank the reviewers the careful reading and the constructive discussions. We gratefully acknowledge the CSCS for providing us the CPU resources under project ID s635 and s796. Part of this work has been developed in the context of ERC Proof of Concept grant MATH4AAAARISK and of the FNS project 200021E-168311, Domain-Decomposition-Based Fluid Structure Interaction Algorithms for Highly Nonlinear and Anisotropic Elastic Arterial Wall Models in 3D. The geometries considered in this study are taken from fully anonymous patients, named AAA₁ to AAA₁₁, as approved by the Ethical committee of the Fondazione IRCCS Ca' Granda - Ospedale Maggiore Policlinico (Aut. 2373 12th April 2013).

Compliance with Ethical Standards Funding: This study was funded by ERC-PoC (grant number 680420) and FNS (grant 200021E-168311).

Conflict of Interest: Chiara Riccobene and Elisa Schenone are employee of the company MOX-OFF; Alfio Quarteroni is co-founder and President of MOXOFF.

References

1. Aggarwal, S., Qamar, A., Sharma, V., Sharma, A.: Abdominal aortic aneurysm: A comprehensive review. *Experimental & Clinical Cardiology* **16**(1), 11–15 (2011). URL <http://www.ncbi.nlm.nih.gov/pmc/articles/PMC3076160/>
2. Airhart, N., Curci, J.: Arterial aneurysms. In: J.J.K. Cronenwett (ed.) *Rutherford's Vascular Surgery*, 8th edn., chap. 9. Elsevier Saunders, Philadelphia (2014)
3. Antiga, L., Piccinelli, M., Botti, L., Ene-Iordache, B., Remuzzi, A., Steinman, D.A.: An image-based modeling framework for patient-specific computational hemodynamics. *Medical & Biological Engineering & Computing* **46**(11), 1097 (2008). DOI 10.1007/s11517-008-0420-1. URL <https://doi.org/10.1007/s11517-008-0420-1>
4. Arzani, A., Suh, G.Y., Dalman, R.L., Shadden, S.C.: A longitudinal comparison of hemodynamics and intraluminal thrombus deposition in abdominal aortic aneurysms. *American Journal of Physiology-Heart and Circulatory Physiology* **307**(12), H1786–H1795 (2014). DOI 10.1152/ajpheart.00461.2014. URL <https://doi.org/10.1152/ajpheart.00461.2014>. PMID: 25326533
5. Assar, A.N., Zarins, C.K.: Ruptured abdominal aortic aneurysm: a surgical emergency with many clinical presentations. *Postgraduate Medical Journal* **85**(1003), 268–273 (2009). DOI 10.1136/pgmj.2008.074666. URL <https://pmj.bmj.com/content/85/1003/268>
6. Ayachit, Utkarsh: *The paraview guide: A parallel visualization application*. Kitware, ISBN 978-1930934306 (2015)
7. Bazilevs, Y., Hsu, M.C., Zhang, Y., Wang, W., Liang, X., Kvamsdal, T., Brekken, R., Isaksen, J.G.: A fully-coupled fluid-structure interaction simulation of cerebral aneurysms. *Computational Mechanics* **46**(1), 3–16 (2010). DOI 10.1007/s00466-009-0421-4. URL <http://dx.doi.org/10.1007/s00466-009-0421-4>
8. Bertagna, L., Deparis, S., Formaggia, L., Forti, D., Veneziani, A.: *The LifeV library: engineering mathematics beyond the proof of concept*. ArXiv e-prints (2017)
9. Bhagavan, D., Di Achille, P., Humphrey, J.D.: Strongly coupled morphological features of aortic aneurysms drive intraluminal thrombus. *Scientific Reports* **8** (2018)

10. Boyd, A.J., Kuhn, D.C.S., Lozowy, R.J., Kulbisky, G.P.: Low wall shear stress predominates at sites of abdominal aortic aneurysm rupture. *Journal of Vascular Surgery* **63**(6), 1613–1619 (2016). DOI <http://dx.doi.org/10.1016/j.jvs.2015.01.040>. URL <http://www.sciencedirect.com/science/article/pii/S0741521415001500>
11. Chaikof, E., et al.: The society for vascular surgery practice guidelines on the care of patients with an abdominal aortic aneurysm. *J Vasc Surg*. 2018 Jan;67(1):2-77.e2. doi: 10.1016/j.jvs.2017.10.044. **67**(1), 2–77 (2018). Doi: 10.1016/j.jvs.2017.10.044.
12. Chaikof, E.L., Dalman, R.L., Eskandari, M.K., Jackson, B.M., Lee, W.A., Mansour, M.A., Mastracci, T.M., Mell, M., Murad, M.H., Nguyen, L.L., Oderich, G.S., Patel, M.S., Schermerhorn, M.L., Starnes, B.W.: The society for vascular surgery practice guidelines on the care of patients with an abdominal aortic aneurysm. *Journal of Vascular Surgery* **67**(1), 2–77.e2 (2018). DOI 10.1016/j.jvs.2017.10.044. URL <http://dx.doi.org/10.1016/j.jvs.2017.10.044>
13. Colciago, C.M., Deparis, S., Quarteroni, A.: Comparisons between reduced order models and full 3d models for fluid–structure interaction problems in haemodynamics. *Journal of Computational and Applied Mathematics* **265**, 120–138 (2014). DOI <http://dx.doi.org/10.1016/j.cam.2013.09.049>. URL <http://www.sciencedirect.com/science/article/pii/S0377042713000509>
14. Colciago, C.M., Forti, D., Deparis, S.: Fluid-structure interaction for vascular flows: From supercomputers to laptops. In: Frei, Holm, Richter, Wick, Yang (eds.) *Fluid-Structure Interaction. Modeling, Adaptive Discretisations and Solvers*, no. 20 in Radon Series on Computational and Applied Mathematics, pp. 237–282. De Gruyter (2017)
15. Darling, R.C., Messina, C.R., Brewster, D.C., Ottinger, L.W.: Autopsy study of unoperated abdominal aortic aneurysms. the case for early resection. *Circulation* **56**(3 Suppl), III161–4 (1977)
16. Di Achille, P., Tellides, G., Figueroa, C.A., Humphrey, J.D.: A haemodynamic predictor of intraluminal thrombus formation in abdominal aortic aneurysms. *Proceedings of the Royal Society A: Mathematical, Physical and Engineering Science* **470**(2172) (2014). URL <http://rspa.royalsocietypublishing.org/content/470/2172/20140163.abstract>
17. Di Achille, P., Tellides, G., Humphrey, J.D.: Hemodynamics-driven deposition of intraluminal thrombus in abdominal aortic aneurysms. *International Journal for Numerical Methods in Biomedical Engineering* pp. n/a–n/a (2016). DOI 10.1002/cnm.2828. URL <http://dx.doi.org/10.1002/cnm.2828>
18. Dryjski, M., Driscoll, J.L., Blair, R.C., McGurrin, M.A., Dagher, F.J., Ceraolo, M.J., O'Donnell, Blackshear, W.M.J.: The small abdominal aortic aneurysm: the eternal dilemma. *J Cardiovasc Surg (Torino)* **35**(2), 95–100 (1994)
19. Dua, M.M., Dalman, R.L.: Hemodynamic influences on abdominal aortic aneurysm disease: Application of biomechanics to aneurysm pathophysiology. *Vascular Pharmacology* **53**(1–2), 11–21 (2010). DOI <http://dx.doi.org/10.1016/j.vph.2010.03.004>. URL <http://www.sciencedirect.com/science/article/pii/S1537189110000510>
20. EPFL, MOXOFF, UNIMI, YOTTACLE: aXurge: the ultimate platform that supports vascular specialists, surgeons and evar device specialists in the treatment of abdominal aortic aneurysms. www.axurge.com
21. Faggiano, E., Formaggia, F., Antiga, L.: An open-source tool for patient- specific fluid-structure vessel mesh generation. In: *Modelling of Physiological Flows (MPF)* (2013)
22. Fedele, M., Faggiano, E., Barbarotta, L., Cremonesi, F., Formaggia, L., Perotto, S.: Semi-automatic three-dimensional vessel segmentation using a connected component localization of the region-scalable fitting energy. In: *2015 9th International Symposium on Image and Signal Processing and Analysis (ISPA)*, pp. 72–77 (2015). DOI 10.1109/ISPA.2015.7306035
23. Figueroa, C.A., Vignon-Clementel, I.E., Jansen, K.E., Hughes, T.J., Taylor, C.A.: A coupled momentum method for modeling blood flow in three-dimensional deformable arteries. *Computer Methods in Applied Mechanics and Engineering* **195**(41), 5685 – 5706 (2006). DOI <http://dx.doi.org/10.1016/j.cma.2005.11.011>. URL <http://www.sciencedirect.com/science/article/pii/S004578250500513X>. John H. Argyris Memorial Issue. Part II
24. Fillinger, M.F., Marra, S.P., Raghavan, M.L., Kennedy, F.E.: Prediction of rupture risk in abdominal aortic aneurysm during observation: Wall stress versus diameter. *Journal of Vascular Surgery* **37**(4), 724–732 (2003). DOI <http://dx.doi.org/10.1067/mva.2003.213>. URL <http://www.sciencedirect.com/science/article/pii/S0741521402753482>
25. Finol, E.A., Amon, C.H.: Blood flow in abdominal aortic aneurysms: Pulsatile flow hemodynamics. *Journal of Biomechanical Engineering* **123**(5), 474–484 (2001). URL <http://dx.doi.org/10.1115/1.1395573>
26. Finol, E.A., Keyhani, K., Amon, C.H.: The effect of asymmetry in abdominal aortic aneurysms under physiologically realistic pulsatile flow conditions. *Journal of Biomechanical Engineering* **125**(2), 207–217 (2003). URL <http://dx.doi.org/10.1115/1.1543991>
27. Formaggia, L., Quarteroni, A., Veneziani, A.: *Cardiovascular mathematics. Modeling, Simulation and Applications*. Springer (2009)
28. Gadowski, G.R., Pilcher, D.B., Ricci, M.A.: Abdominal aortic aneurysm expansion rate: Effect of size and beta-adrenergic blockade. *Journal of Vascular Surgery* **19**(4), 727–731 (2006). DOI 10.1016/S0741-5214(94)70048-6. URL [http://dx.doi.org/10.1016/S0741-5214\(94\)70048-6](http://dx.doi.org/10.1016/S0741-5214(94)70048-6)
29. Geroulakos, G., Nicolaides, A.: Infrarenal abdominal aortic aneurysms less than five centimetres in diameter: the surgeon's dilemma. *Eur J Vasc Surg* **6**(6), 616–622 (1992)
30. Heilmaier, C., Moysidis, T., Weishaupt, D., Kroger, K.: Calcification in smaller and larger infrarenal aneurysmatic abdominal aortas- differences in plaque patterns -. *Angiology: Open Access* **2**(2), 1–5

- (2014). DOI 10.4172/2329-9495.1000129. URL <https://www.omicsonline.org/open-access/calcification-in-smaller-and-larger-infrarenal-aneurysmatic-abdominal-aortas-differences-in-plaque-patterns-2329-9495.1000129.php?aid=26495>
31. Joly, F., Soulez, G., Garcia, D., Lessard, S., Kauffmann, C.: Flow stagnation volume and abdominal aortic aneurysm growth: Insights from patient-specific computational flow dynamics of lagrangian-coherent structures. *Computers in Biology and Medicine* **92**, 98 – 109 (2018). DOI <https://doi.org/10.1016/j.complbiomed.2017.10.033>. URL <http://www.sciencedirect.com/science/article/pii/S0010482517303591>
 32. Kazi, M., Thyberg, J., Religa, P., Roy, J., Eriksson, P., Hedin, U., Swedenborg, J.: Influence of intraluminal thrombus on structural and cellular composition of abdominal aortic aneurysm wall. *Journal of Vascular Surgery* **38**(6), 1283 – 1292 (2003). DOI [https://doi.org/10.1016/S0741-5214\(03\)00791-2](https://doi.org/10.1016/S0741-5214(03)00791-2). URL <http://www.sciencedirect.com/science/article/pii/S0741521403007912>
 33. Les, A.S., Shadden, S.C., Figueroa, C.A., Park, J.M., Tedesco, M.M., Herfkens, R.J., Dalman, R.L., Taylor, C.A.: Quantification of hemodynamics in abdominal aortic aneurysms during rest and exercise using magnetic resonance imaging and computational fluid dynamics. *Annals of Biomedical Engineering* **38**(4), 1288–1313 (2010). DOI 10.1007/s10439-010-9949-x. URL <http://dx.doi.org/10.1007/s10439-010-9949-x>
 34. Lozowy, R., Kuhn, D., Ducas, A., Boyd, A.: The relationship between pulsatile flow impingement and intraluminal thrombus deposition in abdominal aortic aneurysms. *Cardiovasc Eng Technol* **8**(1), 57 (2017)
 35. Martino, E.S.D., Bohra, A., Geest, J.P.V., Gupta, N., Makaroun, M.S., Vorp, D.A.: Biomechanical properties of ruptured versus electively repaired abdominal aortic aneurysm wall tissue. *Journal of Vascular Surgery* **43**(3), 570 – 576 (2006). DOI <https://doi.org/10.1016/j.jvs.2005.10.072>. URL <http://www.sciencedirect.com/science/article/pii/S074152140501921X>
 36. The MathWorks, Inc., Natick, Massachusetts, United States: Matlab Release 2015b
 37. Metaxa, E., Tzirakis, K., Kontopodis, N., Ioannou, C.V., Papaharilaou, Y.: Correlation of intraluminal thrombus deposition, biomechanics, and hemodynamics with surface growth and rupture in abdominal aortic aneurysm—application in a clinical paradigm. *Annals of Vascular Surgery* **46**, 357 – 366 (2018). DOI <https://doi.org/10.1016/j.avsg.2017.08.007>. URL <http://www.sciencedirect.com/science/article/pii/S0890509617309457>
 38. Nichols, W.W., O'Rourke, M.: McDonald's Blood Flow in Arteries - Theoretical, experimental and clinical principles. Arnold (1998)
 39. Nobile, F., Vergara, C.: An effective fluid-structure interaction formulation for vascular dynamics by generalized robin conditions. *SIAM Journal on Scientific Computing* **30**(2), 731–763 (2008). DOI 10.1137/060678439. URL <https://doi.org/10.1137/060678439>
 40. Patel, M.I., Hardman, D., Fisher, C.M., Appleberg, M.: Current views on the pathogenesis of abdominal aortic aneurysms. *J Am Coll Surg* (1995)
 41. Piccinelli, M., Vergara, C., Antiga, L., Forzenigo, L., Biondetti, P., Domanin, M.: Impact of hemodynamics on lumen boundary displacements in abdominal aortic aneurysms by means of dynamic computed tomography and computational fluid dynamics. *Biomechanics and Modeling in Mechanobiology* **12**(6), 1263–1276 (2013). DOI 10.1007/s10237-013-0480-5. URL <http://dx.doi.org/10.1007/s10237-013-0480-5>
 42. Quarteroni, A.: Numerical Modeling of Differential Problems, 3rd ed. edn. Springer (2017)
 43. Quarteroni, A., Valli, A.: Numerical Approximation of Partial Differential Equations. Springer Series in Computational Mathematics. Springer (2008)
 44. Shum, J., Martufi, G., Di Martino, E., Washington, C.B., Grisafi, J., Muluk, S.C., Finol, E.A.: Quantitative assessment of abdominal aortic aneurysm geometry. *Annals of Biomedical Engineering* **39**(1), 277–286 (2011). DOI 10.1007/s10439-010-0175-3. URL <http://dx.doi.org/10.1007/s10439-010-0175-3>
 45. Vande Geest, J.P., Wang, D.H.J., Wisniewski, S.R., Makaroun, M.S., Vorp, D.A.: Towards a noninvasive method for determination of patient-specific wall strength distribution in abdominal aortic aneurysms. *Ann Biomed Eng* **34**(7), 1098–1106 (2006). DOI 10.1007/s10439-006-9132-6
 46. Vergara, C., Van, D.L., Quadrio, M., Domanin, M.: Large eddy simulations of blood dynamics in abdominal aortic aneurysms. *Medical Engineering & Physics* **in press** (2017)
 47. Virag, L., Wilson, J.S., Humphrey, J.D., Karšaj, I.: A computational model of biochemomechanical effects of intraluminal thrombus on the enlargement of abdominal aortic aneurysms. *Annals of Biomedical Engineering* **43**(12), 2852–2867 (2015). DOI 10.1007/s10439-015-1354-z. URL <http://dx.doi.org/10.1007/s10439-015-1354-z>
 48. Vorp, D.A.: Biomechanics of abdominal aortic aneurysm. *Journal of Biomechanics* **40**(9), 1887–1902 (2007). DOI <http://dx.doi.org/10.1016/j.jbiomech.2006.09.003>. URL <http://www.sciencedirect.com/science/article/pii/S002192900600323X>
 49. Vorp, D.A., Lee, P.C., Wang, D.H., Makaroun, M.S., Nemoto, E.M., Ogawa, S., Webster, M.W.: Association of intraluminal thrombus in abdominal aortic aneurysm with local hypoxia and wall weakening. *J Vasc Surg* **34**(2), 291–299 (2001). DOI 10.1067/mva.2001.114813
 50. Vorp, D.A., Lee, P.C., Wang, D.H., Makaroun, M.S., Nemoto, E.M., Ogawa, S., Webster, M.W.: Association of intraluminal thrombus in abdominal aortic aneurysm with local hypoxia and wall weakening. *Journal of Vascular Surgery* **34**(2), 291 – 299 (2001). DOI <https://doi.org/10.1067/mva.2001.114813>. URL <http://www.sciencedirect.com/science/article/pii/S0741521401594288>
 51. Vorp, D.A., Wang, D.H.J., Webster, M.W., Federspiel, W.J.: Effect of intraluminal thrombus thickness and bulge diameter on the oxygen diffusion in abdominal aortic aneurysm. *Journal of Biomechanical Engineering* **120**(5), 579–583 (1998). DOI <https://doi.org/10.1115/1.2834747>
 52. Wang, D.H.J., Makaroun, M.S., Webster, M.W., Vorp, D.A.: Effect of intraluminal thrombus on wall stress in patient-specific models of abdominal aortic aneurysm. *J Vasc Surg* **36**(3), 598–604 (2002)